*Advanced Optical Materials*

ADVANCED OPTICAL MATERIALS
www.advopticalmat.de

RESEARCH ARTICLE OPEN ACCESS

# Luminescence and Photochromism in Lanthanide-Doped Hackmanites

Joshua Baggott[1] | Minnea Tuomisto[1] | J. A. Gareth Williams[2] | Sari Granroth[3] | Ermei Mäkilä[3] | Ari Väisänen[4] | Jani O. Moilanen[4] | Mika Lastusaari[1]

[1]Department of Chemistry, University of Turku, Turku, Finland | [2]Department of Chemistry, Durham University, Durham, UK | [3]Department of Physics and Astronomy, University of Turku, Turku, Finland | [4]Department of Chemistry, University of Jyväskylä, Jyväskylä, Finland

**Correspondence:** Mika Lastusaari (miklas@utu.fi)

**Received:** 30 January 2026 | **Revised:** 16 April 2026 | **Accepted:** 18 May 2026

**Keywords:** hackmanite | lanthanide | luminescence | photochromism

## ABSTRACT

Hackmanites are a class of materials that exhibit diverse and intriguing optical characteristics, including luminescence and tenebrescence. Doping with other luminescent species would unveil a fresh spectrum of optical properties and potential applications. This project aimed to successfully dope a lithium derivative of hackmanite with highly luminescent lanthanides ($Sm^{3+}$, $Eu^{3+}$, $Tb^{3+}$, and $Dy^{3+}$) using a doped aluminosilicate precursor, $LiAlSiO_4$. Initial structural analysis indicated successful doping with little disruption to the host lattice. Luminescence spectroscopy revealed that the emissive properties of the lanthanide ions were largely suppressed upon incorporation into the sodalite due to the presence of other highly luminescent impurities. However, europium-doped samples exhibited emission from both $Eu^{2+}$ and $Eu^{3+}$, with the former resulting in long-lasting green persistent luminescence. Room-temperature persistent luminescence was determined to arise from traps at a depth of 0.3 eV. In contrast, doping with samarium yielded a photochromic response atypical of traditional hackmanites, characterized by absorption extending into the near-infrared region. Spectroscopic evidence suggested the involvement of $Sm^{2+}/Sm^{3+}$ redox processes coupled to disulphide photochromic centers in the tenebrescence mechanism. Lanthanide doping provides a versatile route for modifying both the luminescence and photochromic behavior of hackmanites, enabling additional functionalities in lighting applications and UV dosimetry.

## 1 | Introduction

Photochromism is the light-induced reversible transformation of a chemical species between two different forms with different absorption spectra [1]. Many photochromic materials exist, including organic, inorganic, and hybrid materials [2–4]. Photochromism is also a natural phenomenon. Upon exposure to UV (ultraviolet) radiation, some minerals, such as hackmanite ($Na_8Si_6Al_6O_{24}[Cl, S]_2$), and scapolite ($[Na, Ca]_4Al_3Si_9O_{24}[Cl, CO_3]_2$), exhibit a reversible color change, called tenebrescence by geologists. These minerals belong to the aluminosilicate family, all of which possess a characteristic aluminosilicate cage known as a $\beta$-cage [5, 6]. The photochromism in these minerals requires the replacement of small amounts of $Cl^-$ ions with the divalent $S_2^{2-}$ anion. This substitution leads to charge compensation by creating chloride vacancies ($V_{Cl}$) [7]. The divalent $S_2^{2-}$ anions absorb UV radiation and transfer electrons to the chloride vacancies, creating metastable F-centers that absorb visible wavelengths. Upon heating or exposure to white light, the electrons return to the disulfide ions and restore the material to its original color, known as thermal or optical bleaching, respectively [5, 6].

Apart from occurring in nature, these materials can also be synthesized, albeit more readily for hackmanite than tugtupite

or scapolite [8, 9]. The optical properties of synthetic hackmanite offer a wide range of commercial applications, favored by the ease with which hackmanites can be tuned in composition, as subtle changes in the synthesis procedure allow the incorporation of different ions into the crystal structure.

Significant changes to the material can be achieved by utilizing different alkali metal halides during synthesis, which requires minimal modifications to the synthetic method [7]. Typically, hackmanite is synthesized using NaCl, but replacing it with other alkali metal halides with larger ions (e.g. KBr) generally results in unit cell expansion, increasing the size of the halide vacancy and thus shrinking the HOMO-LUMO energy gap of the F-center [10]. For cations such as $K^+$, an increased ionic radius compared to $Na^+$ was shown to decrease the energy of electron transfer due to a larger vacancy [7]. On the other hand, substituting $Na^+$ with $Li^+$ had the opposite effect, increasing the energy of electron transfer due to its smaller ionic radius of 0.59 Å compared to 0.99 Å for $Na^+$ in a four-coordinate environment [11]. Variation in the halide counterion also influenced the wavelength of the absorbance maximum, increasingly redshifted down the group. This redshift is likely due to the increasing size of the halide anion, which expands the unit cell and thus increases the size of the vacancy, similar to the effect of the alkali metal cation [10, 12]. Combining the effects of both ions provided a significant degree of control over the tenebrescence color of the material, as evidenced by the extensive range of reflectance minima obtained [7]. Mixing a range of these compounds can, for example, result in a mixture with a distinct coloration depending on the wavelength of light present, allowing for use in radiation dosimetry [7].

Hackmanites also exhibit orange luminescence due to the disulfide ($S_2^{2-}$) impurities required for photochromism [13, 14]. These are converted from the dianion to the monoanionic $S_2^-$ upon F-center formation. Electronic transitions in this species from the $^2\Pi_u$ excited state to the $^2\Pi_g$ ground state give rise to this characteristic orange emission upon UV excitation [14].

It has also been reported that it is possible to dope synthetic hackmanite with certain transition metals to enhance its luminescent properties [15]. A prominent example is the range of synthetic hackmanite derivatives doped with $Ti^{3+}$, with the general formula of $[Li_xNa_{1-x}]_8[AlSiO_4]_6[Cl_{1-2y}S_y]$:$z$Ti$^{3+}$ [16]. Excitation of the samples at 310 nm resulted in a broad emission band centerd at approximately 450 nm, attributed to the $Ti^{3+}$ ions substituted into the $Al^{3+}$ tetrahedral sites [17]. The band exhibited asymmetry, suggesting the presence of two overlapping contributions. These were centerd at 452 and 510 nm upon deconvolution, attributed to two distinct $Ti^{3+}$ environments: in $[TiO_4]$ units or $[TiO_4]$-$V_{Cl}$ clusters, and in $[TiO_4]$-$S_2$ units, respectively. The combination of these bands resulted in an overall blue/white appearance. The samples also exhibited persistent luminescence for a significant duration upon removal of the excitation source, with two overlapping contributions at 485 and 570 nm. These can be attributed to the same species as the photoluminescence, causing a similar emission color [17]. The persistent luminescence here results from the trapping of charge carriers, followed by their slow release. These natural impurities enable the material to be used as a self-sustaining lighting solution for appliances such as emergency exit signs [16, 18].

Materials containing lanthanide ions ($Ln^{3+}$) also exhibit a range of exciting properties and applications. Examples include $Y_2O_3$:$Eu^{3+}$ phosphors used in cathode ray tubes, neodymium YAG (Yttrium Aluminum Garnet) lasers, and erbium-doped optical fibers utilized in telecommunications [19–21]. Although lanthanide doping and luminescence have been studied in a plethora of solid-state host materials, only one such study has been reported for hackmanite: doping $Na_8Al_6Si_6O_{24}(Cl,S)_2$ with $Yb^{3+}$ and $Er^{3+}$ was reported to yield a material with weak upconversion luminescence [22]. This was attributed to the lack of suitably sized trivalent sites in the structure, resulting in limited solubility of the lanthanides in the hackmanite lattice. In addition, successful doping of $Eu^{3+}$ and $Tb^{3+}$ to give red and green luminescence, respectively, has been reported for the non-photochromic sodalite, $Na_8Al_6Si_6O_{24}Cl_2$ [23, 24].

Although, to the best of our knowledge, the photochromic behavior of lanthanide-doped hackmanites has not yet been investigated, recent research indicates that lanthanide ions influence the photochromic properties of other inorganic materials. For instance, europium doping has been shown to significantly affect the photochromic mechanisms in doped apatite-like materials ($Sr_5(PO_4)_3F_{1-x}Cl_x$:1%Eu), which utilize $Eu^{2+}$ as a source of photoexcited electrons trapped in created oxygen vacancies, forming F-centers that are further modulated by halide anion substitution; and in ferroelectric ceramics ($K_{0.5}Na_{0.5}NbO_3$-Eu), which employ deep electron traps formed by $Eu^{3+}$ [25, 26]. Additionally, lanthanide and transition metal dopants have been shown to indirectly influence the photochromism color of $BaMgSiO_4$, being used as color dopants to produce an initial body color that subsequently affects the final color after excitation, resulting in a range of multicolor photochromic materials [27].

In this work, lanthanide-doped hackmanites were synthesized using $Ln^{3+}$-doped lithium aluminosilicates ($LiAlSiO_4$) as the starting material, rather than the commonly used zeolite A. This route was chosen because highly luminescent doped lithium aluminosilicates have been previously reported [7, 28, 29]. We aim to show whether the emission from these lanthanides can be retained upon incorporation into photochromic sodalites, as well as how the presence of these dopants influences the luminescence and tenebrescence properties and mechanisms.

In particular, we focus on lanthanide ions that typically emit primarily in the visible region of the electromagnetic spectrum, namely $Sm^{3+}$, $Eu^{3+}$, $Tb^{3+}$, and $Dy^{3+}$ [30–33]. Special attention is paid to the emergence of divalent lanthanide species under the reducing conditions typically used during synthesis, and the deviations from optical behaviors of traditional hackmanites. Using a range of spectroscopic methods, we investigate the role of lanthanide dopants in governing charge trapping, color center dynamics, and their interactions with other impurities typically present in these materials. We aim to demonstrate that lanthanide doping is a viable route to synthesizing hackmanites with multiple optical properties, depending on the chosen dopant, and to provide new insights into the interplay between dopants and defects in these materials.

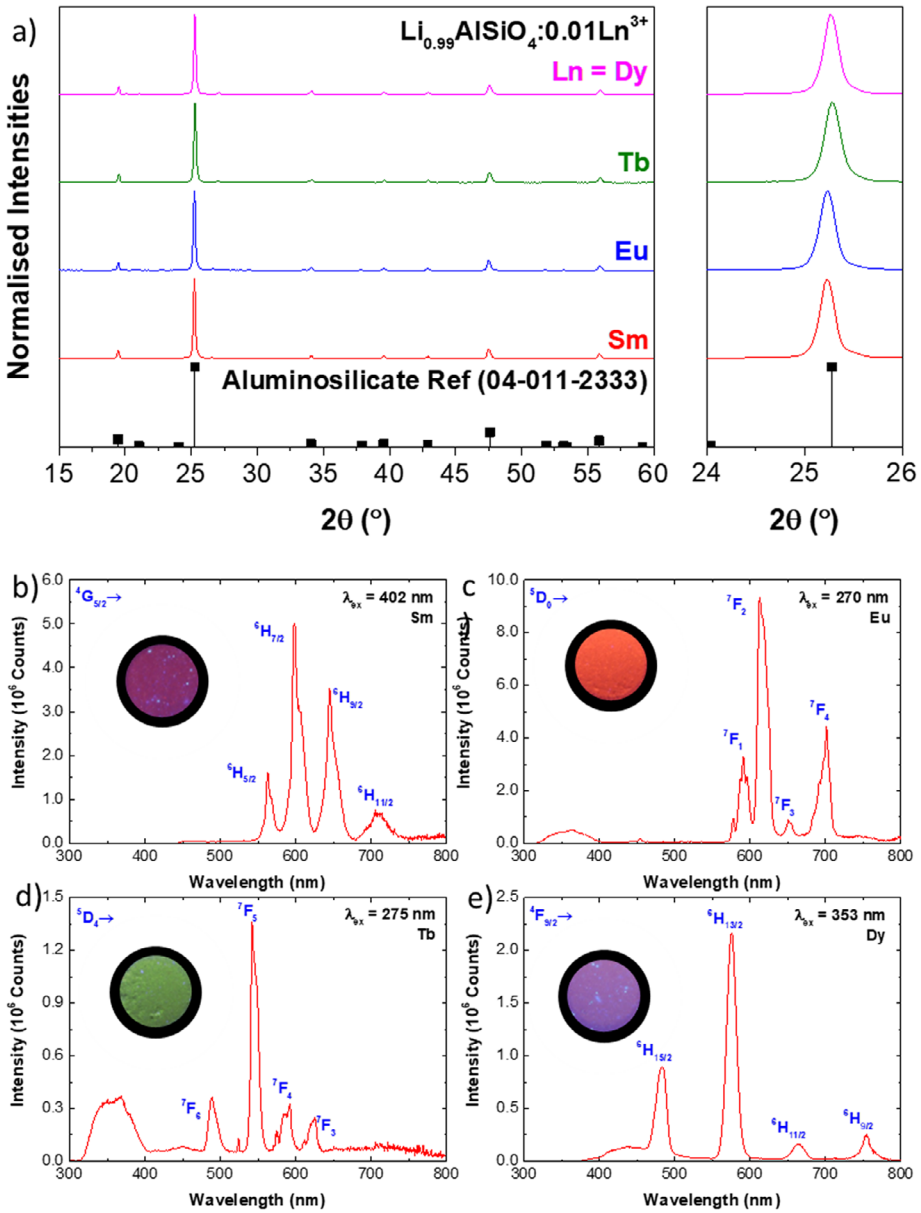


**FIGURE 1** | (a) Normalized XRD pattern of synthesized $LiAlSiO_4$ doped with 1 mol% $Ln^{3+}$ ($Li_{0.99}AlSiO_4$:$0.01Ln^{3+}$), where Ln = Sm, Eu, Tb, Dy, and compared to a simulated reference scan. Note that all experimental curves shown here have been corrected for any errors resulting in $2\theta$ shifts. (b–e) Luminescence spectra of $Li_{0.99}AlSiO_4$:$0.01Ln^{3+}$, where Ln = (b) Sm, (c) Eu, (d) Tb, and (e) Dy. Significant lanthanide emission peaks have been labeled with the responsible transition [30–33]. The circular insets show photographs of the samples when illuminated with hand-held UV lamps (Sm (b) and Dy (e): 365 nm; Eu (c) and Tb (d): 254 nm).

## 2 | Results and Discussion

### 2.1 | Lanthanide-Doped Aluminosilicate Precursors

Initially, lithium aluminosilicates doped with 1 mol% $Ln^{3+}$ were synthesized with the general formula $Li_{0.99}AlSiO_4$:$0.01Ln^{3+}$ (where Ln = Sm, Eu, Tb, or Dy), using $Ln_2O_3$ as the source of $Ln^{3+}$. The procedure is described in the Experimental Section. There is little change in the shape of the XRD (X-ray diffraction) patterns recorded upon doping with $Ln^{3+}$ compared to that of undoped $LiAlSiO_4$ (Figure 1a). This lack of change demonstrates that adding sufficient $Ln_2O_3$ to the starting materials to achieve 1 mol% doping does not result in significant changes in the morphology of the final product, confirming the likely suitability of these materials as precursors to doped sodalites. Additionally, even though the ionic radii of the $Ln^{3+}$ ions in a 6-fold coordination environment ($Sm^{3+}$ 0.958, $Eu^{3+}$ 0.947, $Tb^{3+}$ 0.923, and $Dy^{3+}$ 0.912 Å) are larger than those of $Li^+$ in a similar 6-fold coordination environment (0.76 Å), their low concentration within the material results in negligible expansion of the unit cell parameter and, thus, an indiscernible shift in the diffraction peaks [11]. As a result of the $Ln^{3+}$ ions replacing $Li^+$, oxygen-related defect centers or $Li^+$ vacancies are likely to be created for charge balancing. As a result, it can be inferred that dopant ions will be in a structurally disordered environment [34]. While there may be a high degree

**TABLE 1** | Summary of the observed $Ln^{3+}$ f-f emission lines in the luminescence spectra in Figure 1b–e.

| $Ln^{3+}$ | Emission wavelength [nm] | Assigned transition |
|---|---|---|
| Sm (b) [30] | 563 | $^4G_{5/2} \rightarrow {}^6H_{5/2}$ |
| | 598 | $^4G_{5/2} \rightarrow {}^6H_{7/2}$ |
| | 645 | $^4G_{5/2} \rightarrow {}^6H_{9/2}$ |
| | 709 | $^4G_{5/2} \rightarrow {}^6H_{11/2}$ |
| Eu (c) [31] | 584 | $^5D_0 \rightarrow {}^7F_0$ |
| | 591 | $^5D_0 \rightarrow {}^7F_1$ |
| | 613 | $^5D_0 \rightarrow {}^7F_2$ |
| | 651 | $^5D_0 \rightarrow {}^7F_3$ |
| | 701 | $^5D_0 \rightarrow {}^7F_4$ |
| Tb (d) [32] | 488 | $^5D_4 \rightarrow {}^7F_6$ |
| | 543 | $^5D_4 \rightarrow {}^7F_5$ |
| | 592 | $^5D_4 \rightarrow {}^7F_4$ |
| | 625 | $^5D_4 \rightarrow {}^7F_3$ |
| Dy (e) [33] | 483 | $^4F_{9/2} \rightarrow {}^6H_{15/2}$ |
| | 575 | $^4F_{9/2} \rightarrow {}^6H_{13/2}$ |
| | 664 | $^4F_{9/2} \rightarrow {}^6H_{11/2}$ |
| | 754 | $^4F_{9/2} \rightarrow {}^6H_{9/2}$ |

of confidence in the positions of the lanthanide ions, high-quality neutron and/or synchrotron diffraction data would be needed to confirm the atomic positions. Such data were unobtainable at the time this research was conducted, but XRF (X-ray fluorescence) spectroscopy was used to verify the presence of lanthanides in the samples (Figure S1).

Luminescence spectra of the samples showed the expected f-f emission lines for each dopant, as indicated in Figure 1b–e) and summarized in Table 1. These transitions show that the incorporation of $Ln^{3+}$ ions into the aluminosilicate precursor materials does not quench their emission. Hence, it seemed likely that their incorporation into sodalite structures would be equally plausible, as addressed in the next section.

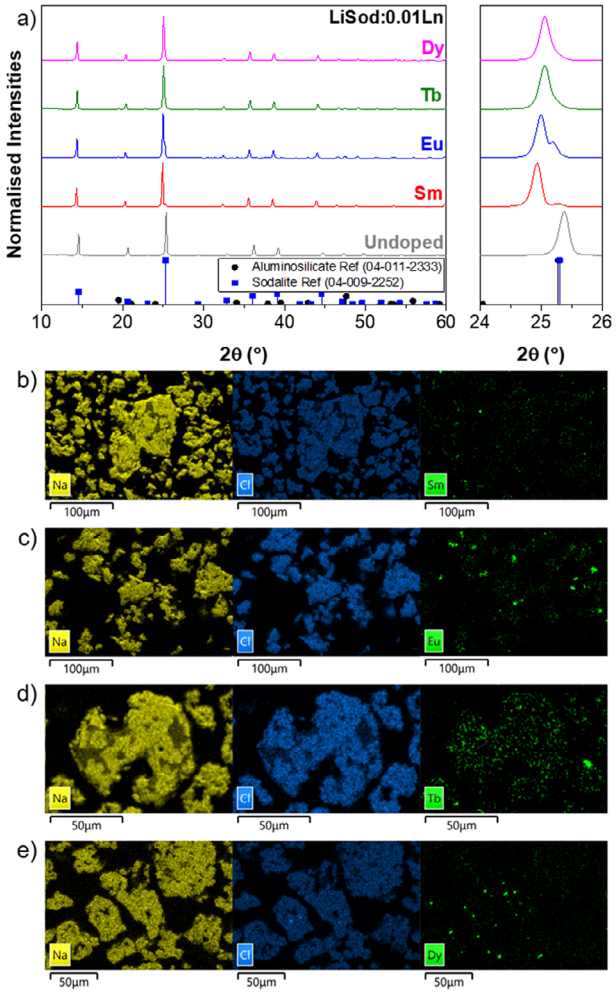


**FIGURE 2** | (a, left) Normalized XRD patterns of sodalite samples LiSod:0.01Ln, where Ln = Sm, Eu, Tb, Dy. These patterns are compared with those of an undoped lithium sodalite sample and simulated reference scans. (a, right) Expansion of the (211) diffraction peak to highlight the shifts in 2$\theta$ values upon alteration of the lanthanide dopant [36]. Note that all experimental curves shown here have been corrected for any errors resulting in 2$\theta$ shifts. (b–e) EDS maps of samples of lithium sodalite doped with 1 mol% $Ln^{3+}$, showing the distribution of sodium, chloride, and lanthanide (Sm, Eu, Tb, and Dy) throughout the sample. Images were obtained using an acceleration voltage of 15 kV and a dwell time of 1 ms. Note, however, that the brightness and contrast of the lanthanide EDS maps have been increased to better visualize their distribution. This is due to the small amount present in each sample being on the edge of the detection range for the apparatus.

## 2.2 | Lanthanide-Doped Hackmanites

### 2.2.1 | Purity

The hackmanites in this section were synthesized from the lithium aluminosilicates described in the previous section. Details are given in the Experimental Section. The XRD patterns of the doped sodalites with the general formula $[Na,Li]_{7.94}[AlSiO_4]_6[Cl,S]_2$:0.01$Ln^{3+}$, henceforth denoted LiSod:0.01Ln, show a strong resemblance to that of the undoped sodalite (Figure 2a), indicating that the presence of lanthanide ions does not result in significant changes to the morphology of the final product. The additional shoulder peak at 25.3° 2$\theta$ in the patterns for the Sm and Eu doped sodalites was found to originate from unreacted aluminosilicate precursor ($Li_{0.99}AlSiO_4$:0.01$Ln^{3+}$, see the reference pattern in Figure 1a). The major difference between the patterns of non-doped and doped materials is the overall shift of the peaks toward lower 2$\theta$ values, indicating a slight unit-cell expansion. This shift in the diffraction peaks indicates successful doping. A slight increase in the unit cell parameter is to be expected upon lanthanide doping due to the larger ionic radii of the $Ln^{3+}$ ions ($Sm^{3+}$ 0.958, $Eu^{3+}$ 0.947, $Tb^{3+}$ 0.923, and $Dy^{3+}$ 0.912 Å) compared to 4-coordinate $Li^+$ (0.59 Å) [11]. This contrasts with the minimal change observed for the doped aluminosilicate precursors, where the $Li^+$ is in a larger, 6-coordinate site, more comparable to $r(Ln^{3+})$. The

quoted $Ln^{3+}$ ionic radii in Section 2.1 are for a 6-coordinate environment, and they are expected to be slightly smaller in the current structures (4-coordinate sites). Estimates of the 4-coordinate $Ln^{3+}$ ionic radii (Table S1) were calculated using calibration curves constructed from radii in higher coordination environments and fit to a straight line (Figure S2). Rietveld refinements were performed on these patterns to calculate the unit cell parameters, *a*, summarized in Table S2. These calculated unit cell parameters correlate with the size of the lanthanide dopant, providing further evidence of successful doping.

The elemental maps obtained by SEM-EDS (Scanning electron microscopy - energy dispersive spectroscopy) also show that the lanthanides are distributed relatively evenly throughout the sample, confirming the successful incorporation into the sodalite structure. However, the images also show regions of higher lanthanide concentration, implying that not all have been fully incorporated. As with the doped aluminosilicates, it can be argued here, with similar reasoning, that the lanthanide impurities occupy $Li^+/Na^+$ sites rather than interstitial or other cationic sites. Again, high-quality synchrotron data would be needed to confirm this hypothesis.

### 2.2.2 | Luminescence

Luminescence spectroscopy was used to verify whether the lanthanide emission was preserved during the transformation of aluminosilicate into sodalite, using the same method as for previous samples. The resulting spectra are displayed below in Figure 3.

The spectra recorded upon excitation at nine different wavelengths in the range 250–410 nm are dominated by emissions other than those from $Ln^{3+}$ ions, irrespective of $\lambda_{ex}$ (Figure 3). It seems that $Sm^{3+}$ emission bands are not present at all (Figure 3a), but weak, diagnostic bands associated with $Eu^{3+}$ (592, 615, and 702 nm; Figure 3b), $Tb^{3+}$ (417, 438, 543, 590, and 622 nm; Figure 3c), and $Dy^{3+}$ (575 nm; Figure 3d) can be observed. One potential hypothesis explaining the low intensity of lanthanide emission is the presence of a reducing atmosphere during the second heating step. Typically, this facilitates the formation of the desired $S_2^{2-}$ dopants that are responsible for tenebrescence in traditional hackmanites. They are precursors to the $S_2^-$ ions that cause the orange luminescence observed upon excitation with lower-energy UV radiation (330–410 nm) as mentioned previously [13, 14]. Indeed, we observe the orange disulfide emission exhibiting S—S vibronic fine structure for each sample.

It is possible that $Ln^{3+}$ ions were reduced to $Ln^{2+}$ as a side effect of the reducing conditions. Based on the reduction potentials of the $Ln^{3+}/Ln^{2+}$ redox couples, $Eu^{3+}$ should be the easiest to reduce to $Eu^{2+}$ [37]. To the knowledge of the authors, $Eu^{2+}$ emission has not been reported previously in sodalite or hackmanite, but here we do observe a broad band from 400 to 700 nm that we suggest is due to $Eu^{2+}$, overlapped with the disulfide emission. This will be discussed more in Section 2.2.3 below. The remainder of the observed emission bands are due to conventional impurities that are typical both in natural and synthetic hackmanite (unless synthesized from ultrapure precursors): $Ti^{3+}$ or $TiO_6$ (ca. 400 nm), $Mn^{2+}$ (510 nm), as well as $Fe^{3+}$ and/or $Cr^{3+}$ (650–750 nm) [14, 38, 39].

### 2.2.3 | Persistent Luminescence of $Eu^{2+}$

The optimal Eu concentration for maximum emission intensity in the Li-sodalite host was determined by investigating compositions varying from 2 to 6 mol% Eu. The compositions of these materials were determined using XRF spectroscopy, with the results shown (expressed as % or ppm by atomic percentage) in both Figure S3 and Table S3. Each sample crystallized mostly in the sodalite phase, but traces of the aluminosilicate phase were observed for the samples with the lowest Eu concentrations (Figure 4a). With 250 nm excitation (i.e. at the $O^{2-}$ to $Eu^{3+}$ charge transfer transition wavelength), it was observed that the $Eu^{2+}$ 5d-4f emission was strongest for the lowest Eu concentrations (Figure 4b,c). Similarly, in the excitation spectra (Figure 4d), the $Eu^{2+}$ 4f-5d excitation band, peaking at 350 nm, is most intense for the lowest Eu concentration, whereas the $Eu^{3+}$ f-f lines dominate at higher Eu concentrations. As an example, pure $Eu^{2+}$ 5d-4f emission was obtained from the 2 mol% sample upon excitation at 350 nm, peaking in the green region at 545 nm (Figure 4e). The band at 250 nm in the excitation spectra (Figure 4d) is due to the $O^{2-}$ to $Eu^{3+}$ charge transfer transition mentioned above and is within the range typically observed for $Eu^{3+}$-doped aluminates and silicates [40].

These Eu-doped Li-sodalites also showed persistent luminescence peaking between 525 and 545 nm, after excitation at 365 nm for 5 min with a hand-held UV lamp (Figure 5a). The apparent variation in $\lambda_{max}$ is due to the spectra being recorded with a monochromator, which scans from the shortest to the longest wavelength. Even if the whole scan takes only 3 s, the fading of the persistent emission will affect the observed peak wavelength, i.e., the faster the fading, the shorter $\lambda_{max}$ will appear to be. Here, the strongest and longest-lasting persistent luminescence was observed in the 0.02Eu sample, whereas the 0.04Eu sample exhibited the shortest duration (Figure 5b). The former has the shortest observed peak wavelength, while the latter has the longest. The decays were recorded to the standard sensitivity limit of a dark-adapted human eye (1% of 0.3 mcd $m^{-2}$), and the fading times to that limit varied from ca. 2 to 40 min (Table 2), in which the 0.02Eu sample showed the longest decay time [41]. With further optimizations, these long decay times present an opportunity for this material to be used in similar applications to those of other persistent luminescent materials, such as emergency exit signs [16].

Figure 5c shows the thermoluminescence (TL) glow curves for the Eu-doped Li-sodalites. The Eu concentrations 2% and 3% clearly show two main maxima centered at approximately 150°C and 325°C, or 200°C and 350°C, respectively. The other Eu concentrations (4%–6%) resulted in only one main maximum at around 150°C–175°C. The Li-sodalite with 2% Eu showed the strongest TL intensity, and so this sample was further studied with the pre-heating method and subsequent initial rise analysis: The TL intensity was recorded after preheating the sample to 50°C, 100°C, 150°C, 200°C, 250°C, and 300°C (Figures S4–S10), and the plots of ln[TL intensity] vs. 1 / T (Figure S11–S17) were used to

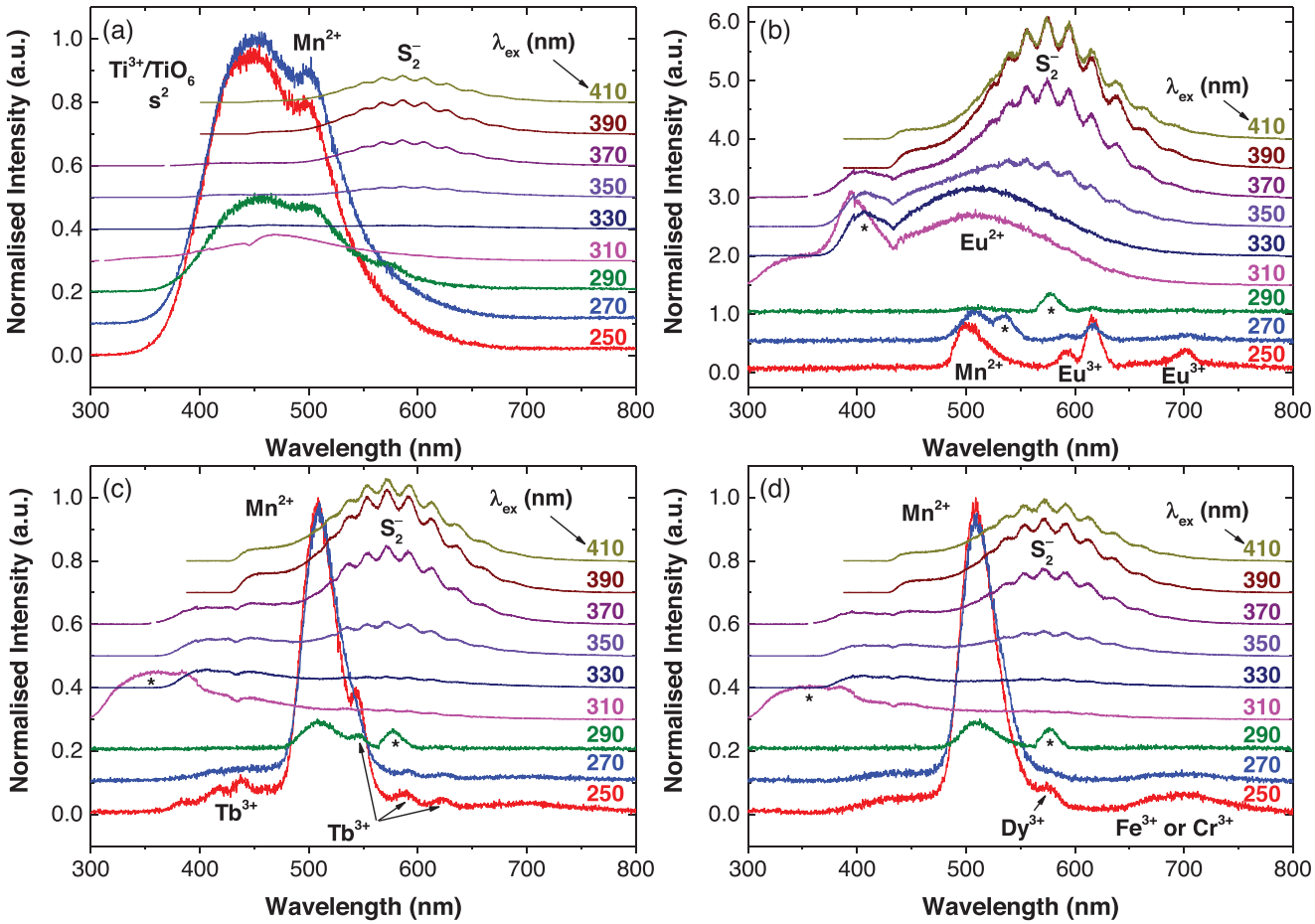


**FIGURE 3** | Luminescence spectra of sodalite samples LiSod:0.01Ln, where Ln = (a) Sm, (b) Eu, (c) Tb, and (d) Dy, upon excitation at the wavelengths. Peaks labelled with an asterisk (*) originate from excitation harmonics.

calculate the trap depths shown in Figure 5d. The trap depth vs. preheating temperature curve (Figure 5d) shows two plateaus at 0.3 and 2.2 eV, which correspond to the two TL glow curve bands (Figure 5c).

The observation that the $O^{2-}$ to $Eu^{3+}$ charge transfer transition is at 250 nm (4.95 eV) indicates that the $Eu^{2+}$ 4f ground state ($^8S_{7/2}$) is located 4.95 eV above the valence band [40]. Furthermore, knowing that the experimentally determined band gap for hackmanite is reported to be 7.7 eV places the 4f ground state 2.75 eV below the conduction band (Figure 5d) [17]. Given that the 4f-5d excitation band is observed from 475 to below 300 nm, i.e. 2.6 to 4.1 eV (Figure 4d), there is a considerable overlap between the 5d states and the conduction band. The overlap allows the excited electron to escape into the conduction band. Then, the persistent luminescence mechanism may comprise the following steps, and is represented schematically in Figure 5e: (1) When the $Eu^{2+}$ is excited with sufficient energy to reach the 5d states that overlap with the conduction band, the excited electron escapes into the conduction band. (2) Escaped electrons can reach nearby trap levels near the conduction band (observed with thermoluminescence) and become trapped. (3) Thermal energy available at room temperature raises the trapped electron back to the conduction band. In this case, the shallower trap (Trap 1; 0.3 eV) is likely responsible for the persistent luminescence, whereas the deeper trap (Trap 2; 2.2 eV) is too deep to be depopulated by thermal energy at room temperature. (4) The electron finds the 5d states of $Eu^{2+}$ again. (5) The electron first relaxes back down to the lowest 5d states and then to the 4f ground state, emitting persistent luminescence at approximately 545 nm in the process.

### 2.2.4 | Photochromism

As previously noted, hackmanite derivatives are renowned for their photochromic properties, particularly their ability to change color upon exposure to UV radiation known as tenebrescence, which can be modified through subtle compositional modifications [6, 7, 17, 18]. Reflectance spectroscopy was employed to assess whether analogous behavior was observed in these lanthanide-doped hackmanite derivatives. The reflectance spectra acquired for each of the 1 mol% Ln sodalite samples (LiSod:0.01Ln) are presented in Figure 6a. The Eu-doped sodalite sample (LiSod:0.01Eu) exhibited no change in reflectance, whereas the Tb and Dy-doped samples (LiSod:0.01Tb and LiSod:0.01Dy, respectively) exhibited a negligible reflectance valley. Additionally, no color change was visible with these samples. However, the Sm-doped sodalite sample (LiSod:0.01Sm) was the only one to demonstrate a significant reflectance valley upon UV exposure and the sole sample to exhibit a visible color change

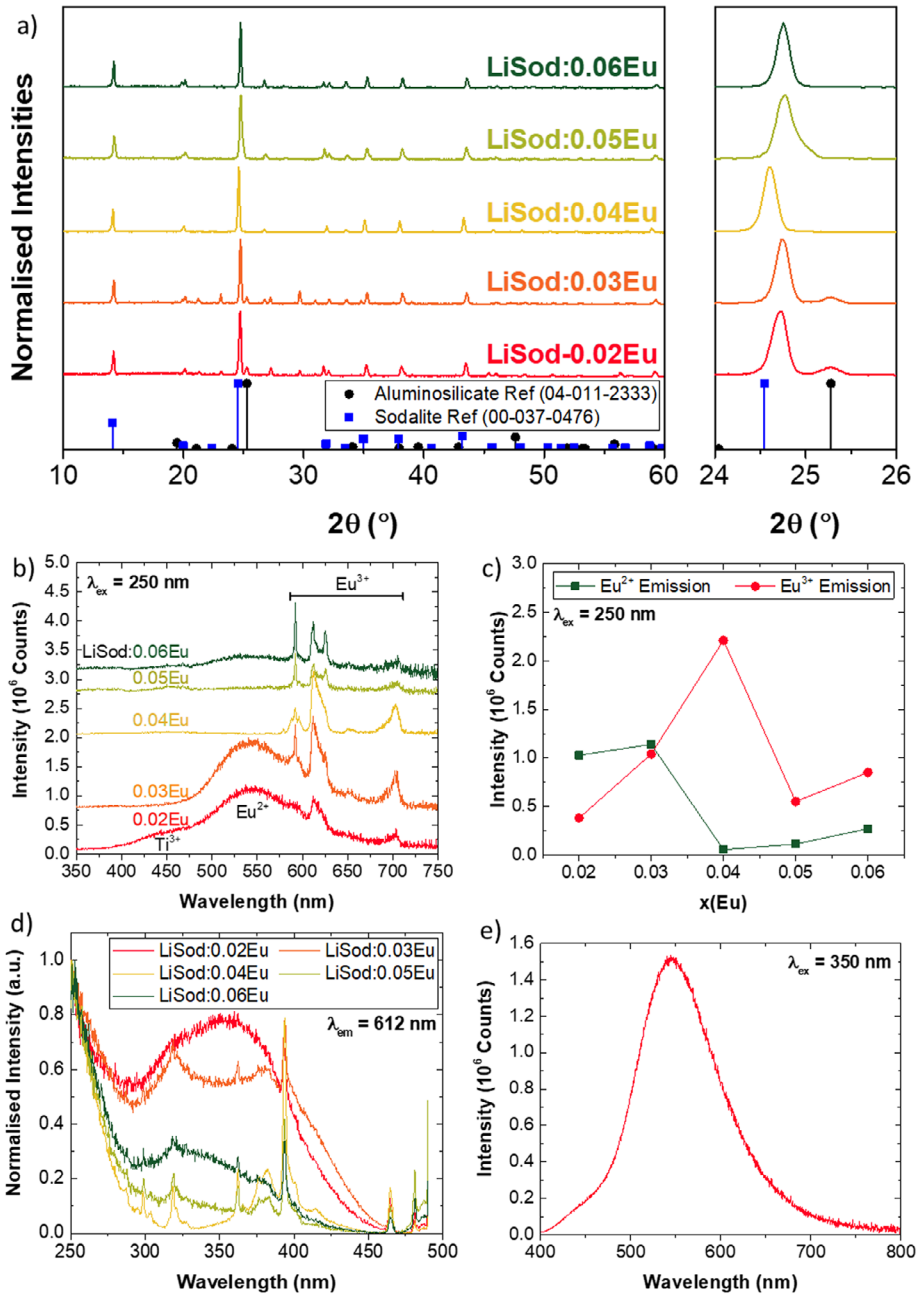


**FIGURE 4** | (a) Normalized XRD patterns of Eu sodalite samples compared with simulated reference scans. The expansion of the sodalite (211) diffraction peaks on the right highlights the possible presence of the aluminosilicate phase [36]. Note that all curves shown here have been corrected for any errors resulting in 2$\theta$ shifts. (b) Photoluminescence emission spectra obtained with 250 nm excitation. (c) Variation of the $Eu^{2+}$ and $Eu^{3+}$ emission intensities as a function of Eu content. (d) Photoluminescence excitation spectra recorded at 612 nm. (e) Photoluminescence emission spectrum obtained for the LiSod:0.02Eu sample with 350 nm excitation.

(Figure 6a, inset). Consequently, this sample was selected for subsequent measurements.

In contrast to conventional hackmanite derivatives, which display reflectance minima in the visible range, this material shows a reflectance minimum at approximately 770 nm, with the valley extending into the near-infrared (NIR) range [7]. For the regular photochromism in hackmanite, the peak energy of the absorption of the colored form, $E_{abs}$, is dependent on the size of the chloride vacancy, $d_{vac}$, forming the color center. That is, the log($E_{abs}$) vs. log($d_{vac}$) correlation is linear [42, 43]. The $d_{vac}$ can be calculated using the Na-Cl distance ($d_{Na\text{-}Cl}$) and the ionic radius of the cation in the Na site ($r_{Na}$, Equation 1) [42].

$$d_{\mathrm{vac}} = \frac{2\left(d_{\mathrm{Na-Cl}} - r_{\mathrm{Na}}\right)}{\sqrt{3}} \quad (1)$$

Here, the observed unit cell parameter value (approximately 8.68 Å; Table S2) suggests that the distance between the Na and Cl sites is 2.673 Å, assuming the regular hackmanite crystal structure [44]. Based on the data reported previously, there is a linear correlation between the Na/Li ratio and the unit cell parameter

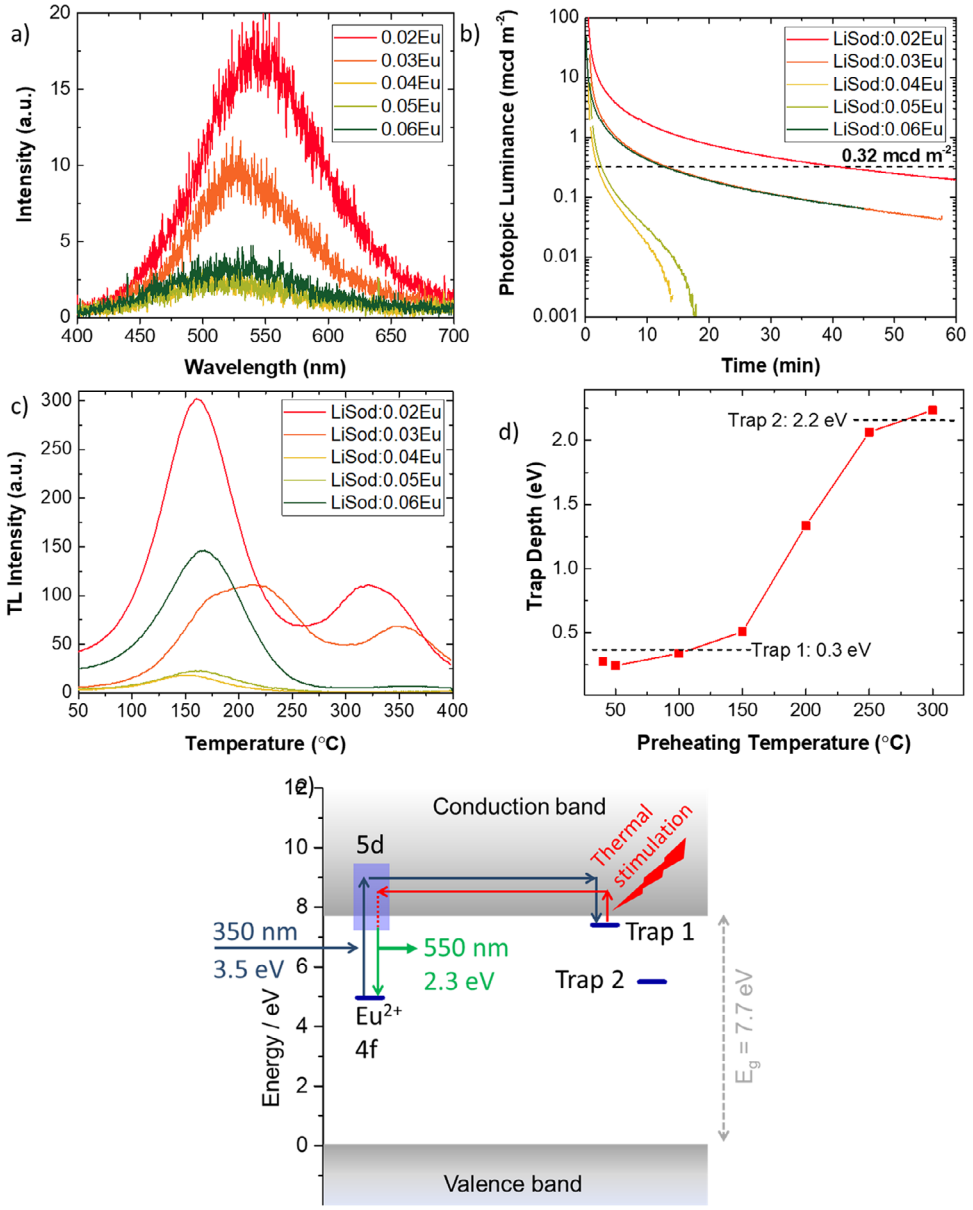


**FIGURE 5** | (a) Persistent luminescence spectra of $Eu^{2+}$ sodalites. (b) Emission decay curves of $Eu^{2+}$ sodalite samples. (c) Thermoluminescence glow curves for Eu-doped Li-sodalites. (d) Trap depth vs. preheating temperature for LiSod:0.02Eu. (e) Persistent luminescence mechanism.

**TABLE 2** | Time taken for the luminescence intensity of the $Eu^{2+}$ sodalite samples to reach the standard photopic limit of 0.32 mcd $m^{-2}$ [41].

| Sample | Time [min] |
|---|---|
| LiSod:0.02Eu | 40.9 |
| LiSod:0.03Eu | 13.2 |
| LiSod:0.04Eu | 2.0 |
| LiSod:0.05Eu | 2.6 |
| LiSod:0.06Eu | 12.8 |

value [45, 46]. For our Sm-doped material, the observed unit cell parameter suggests a Na/Li ratio of 4.12/3.88 (Figure S23). Based on the tabulated ionic radii for four-coordinate $Li^+$ and $Na^+$, the average ionic radius at the Na site can be assumed to be 0.796 Å [11]. This indicates a vacancy size of 2.168 Å, from which an absorption maximum at 600 nm would be predicted, as opposed to the observed 770 nm. This deviation from the expected value could be due to experimental uncertainties in the correlation model or to the photochromic species not being the same as in regular hackmanite.

To investigate the tenebrescence mechanism in our material, we recorded a color rise curve under a regular hand-held 254 nm UV lamp (Figure 6b). The overall shape of the rise curve is similar to those of previously reported hackmanite derivatives [7], although saturation occurs more slowly. These derivatives demonstrated saturation after a cumulative UV dose of approximately 1.5 J $cm^{-2}$, indicating that all possible F-centers have formed. In contrast, our LiSod:0.01Sm sample exhibited saturation at more than twice that UV dose, around 4 J $cm^{-2}$. The slower rate of coloration may suggest an alternative tenebrescence mechanism compared

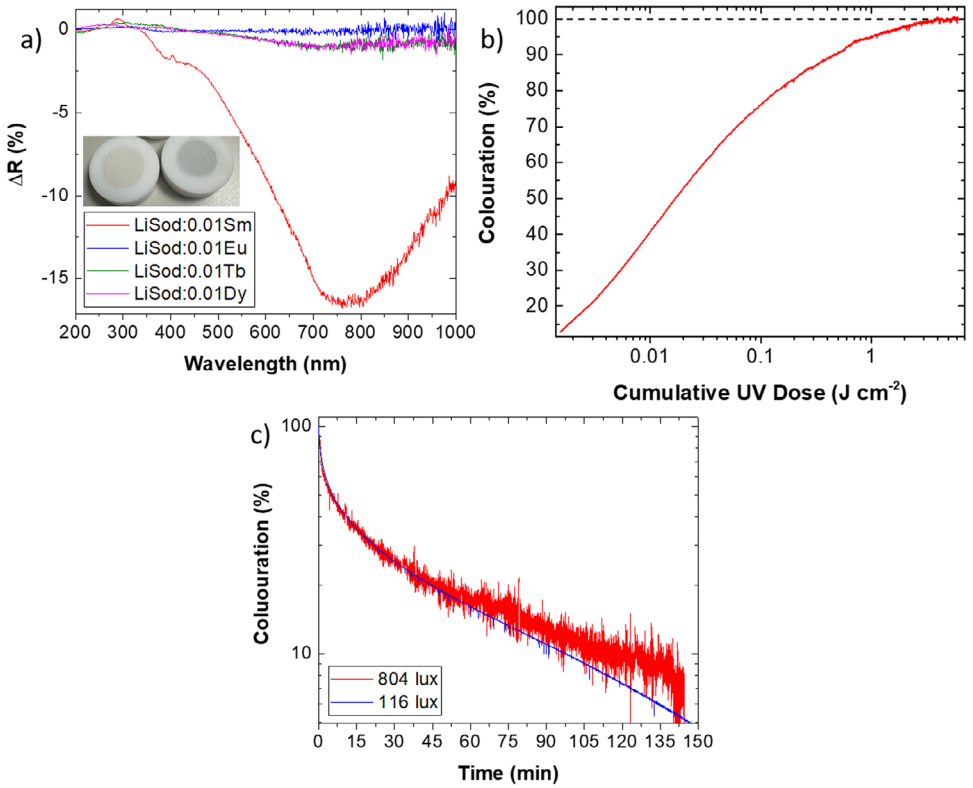


**FIGURE 6** | (a) Reflectance spectra of sodalites samples LiSod:0.01Ln, where Ln = Sm, Eu, Tb, and Dy. The inset shows an image of sample LiSod:0.01Sm before (left) and after (right) 5 min of excitation at 254 nm. (b) Tenebrescence rise curve for sample LiSod:0.01Sm as a function of UV dose. The sample was measured under 254 nm UV radiation with an intensity of 1 mW $cm^{-2}$. (c) Tenebrescence bleaching decay curves for sample LiSod:0.01Sm. The sample was bleached under ambient LED ceiling lights (red) with an intensity of 804 lux and a halogen light source (blue) with an intensity of 116 lux. The spectra of these light sources are shown in Figure S18.

to more conventional hackmanite derivatives. This hypothesis is further supported by the color bleaching curves in Figure 6c that were obtained under ambient LED (ligh-temitting diode) ceiling lights with an intensity of 804 lux and a halogen light source of 116 lux. The curves show almost identical coloration decays under these two white sources, which have very different illuminance and spectra (Figure S18). This suggests that, unlike in the regular hackmanite tenebrescence mechanism, optical bleaching of color does not occur. Furthermore, here the tenebrescence diminishes tri-exponentially rather than bi-exponentially, as observed in previously reported hackmanite derivatives [47]. An example tri-exponential fit is shown in Figure S20 and Table S4.

To gain further insight into the tenebrescence mechanism in this Sm-doped hackmanite derivative (LiSod:0.01Sm), the thermotenebrescence (TT) technique was employed (Figure 7a). This method was developed to observe color bleaching in photochromic materials by measuring their reflectance as a function of temperature [18, 43]. Applying the initial rise method to the curve in a similar fashion to TL curves, it was possible to calculate the energy required to bleach the material (Figure S22) [18, 48]. The results indicate three different thermal bleaching energies: 0.06, 0.13, and 0.53 eV. The lowest of these energies is sufficiently low, i.e., it corresponds to the thermal energy available at room temperature, to confirm that the bleaching shown in Figure 6c is of thermal origin rather than optical.

Since the results above suggest that the tenebrescence mechanism is not the same as for regular hackmanites, we investigated the possible participation of the Sm dopant in the mechanism by employing XPS (X-ray photoelectron spectroscopy) measurements before and after UV exposure (Figure 7b). We observed the $Sm^{3+}$ $3d_{5/2}$ signal at 1083 eV [49, 50]. This also indicates that even if no $Sm^{3+}$ photoluminescence was observed for this sample, the element itself is indeed present. The $3d_{5/2}$ signal for $Sm^{2+}$ has been reported to be at 1072 eV, which is unfortunately coincident with that of the $Na^+$ 1s signal, also observed [49–51]. However, our results show that the intensity of the $Sm^{3+}$ signal decreases with respect to that of $Na^+$, which suggests that the $Sm^{3+}$ concentration decreases concomitantly with an increase in $Sm^{2+}$ concentration. Thus, samarium may participate in the tenebrescence mechanism.

The theories for photochromism in lanthanide-doped materials are not very well established. Generally, it is known that there are three main types of processes: (1) The lanthanide is not associated with the actual photochromic center (PC). (2) The lanthanide is coupled with a PC, and an electron transfer between the lanthanide and the PC results in photochromism. (3) Two different lanthanides form a redox pair with an electron transfer between the lanthanides causing the color changes [52].

Since, in the present case, we have only one lanthanide dopant and photochromic behavior is not the same as that of regular hackmanite, process 2 should apply. Given this, let us first assume

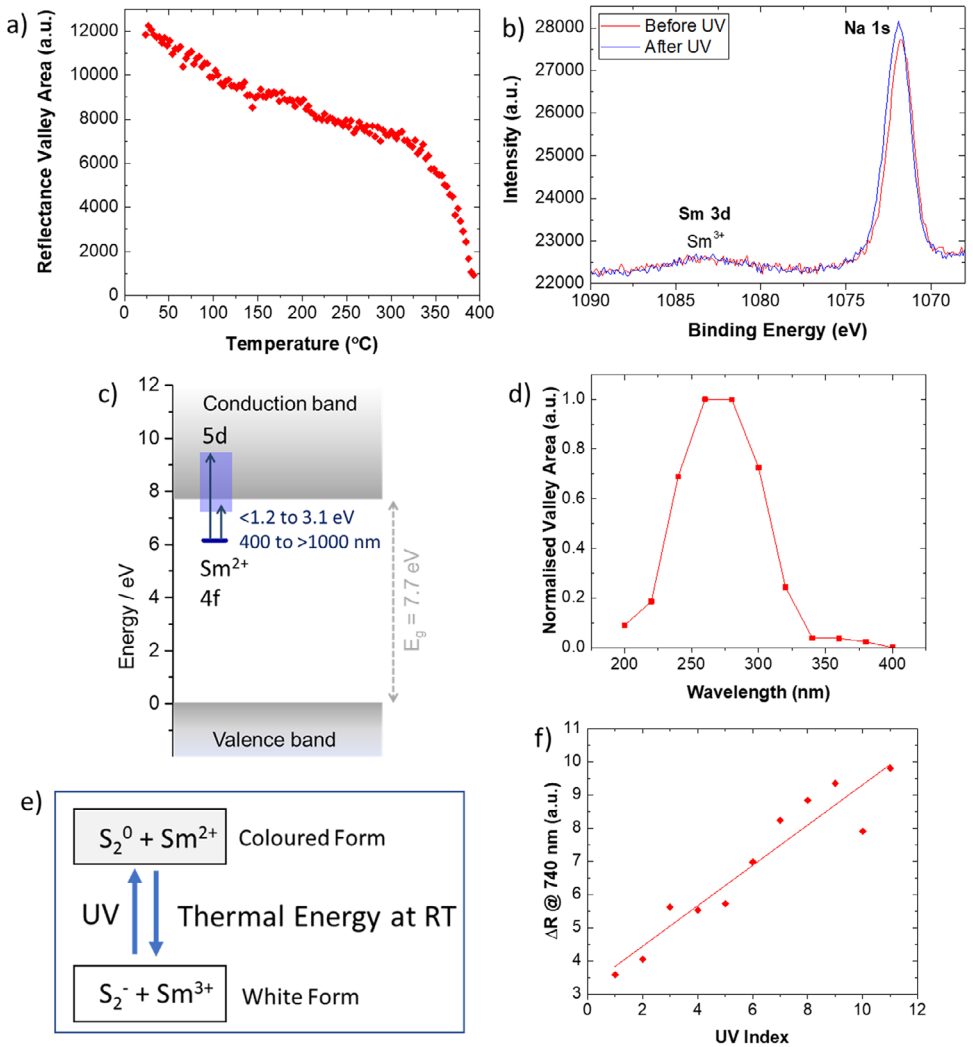


**FIGURE 7** | (a) Thermotenebrescence (TT) curve for sample LiSod:0.01Sm. (b) Na 1s and Sm 3d XPS spectra before and after UV exposure. (c) Location of $Sm^{2+}$ 4f and 5d states in the band gap of hackmanite. (d) Normalized tenebrescence excitation spectrum for sample LiSod:0.01Sm. (e) Proposed tenebrescence mechanism for Sm-doped hackmanite. (f) Reflectance minima of sample LiSod:0.01Sm after 5 min of excitation with solar radiation with various UV indices.

that we already have the $Sm^{2+}$ ion formed by electron transfer from the PC species, thereby creating a $PC^+$ species. The location of the $Sm^{2+}$ 4f ground state within the band gap can be estimated by noting that it typically lies approximately 1.2 eV above that of $Eu^{2+}$ [40]. This means it is 6.15 eV above the valence band and 1.55 eV below the conduction band. The 1.55 eV energy difference corresponds to a wavelength of 800 nm, which is very close to the reflectance minimum of 770 nm (1.61 eV) that we observed experimentally. Knowing that the bottom of the conduction band of hackmanite consists primarily of the 3s and 3p orbitals of Al and Si, the allowed 4f($Sm^{2+}$) to 3s($Al^{3+}$) and/or 3s($Si^{4+}$) transitions could be the origin of the photochromic color. Another possibility is the 4f-5d transition of $Sm^{2+}$ [53]. According to Dorenbos, the location of the lowest 5d state with respect to the conduction band changes minimally between different divalent lanthanides [54]. Therefore, we can assume that the 5d orbitals are located at the same energy with respect to the conduction band as those of $Eu^{2+}$. This places them as shown in Figure 7c. Since the reflectance spectrum in Figure 6a suggests that the absorption band of the colored form extends from 400 to above 1000 nm, the colored form absorbs energies from below 1.2 to 3.1 eV. Because of the clear upper energy limit for the absorption, it seems that the 4f to 5d absorption is a more probable mechanism for the absorption of the colored form than the mechanism involving absorption from the 4f orbitals to the conduction band. With the help of thermal energy at room temperature and the overlap of the 5d band with the conduction band, the escape of electrons from $Sm^{2+}$ to the conduction band is facilitated. The subsequent return of the electron to the $PC^+$ species results in the formation of $Sm^{3+}$ and PC.

However, the exact nature of the PC species remains an open question. The tenebrescence excitation spectrum (Figure 7d) peaks at ca. 275 nm and appears to have a band as expected for hackmanites, and the peak wavelength is in the range that is very typical of hackmanites [17]. Furthermore, the disulfide emission is about 15% weaker in the colored than in the white form (Figure S21), which suggests a decrease in the concentration of $S_2^-$ ions. Removing an electron from $S_2^-$ would create $S_2^0$, which is also a luminescent species. It typically emits a peak at

385 nm, shows similar vibrational fine structure to $S_2^-$, and is best excited at 280 nm [55]. For the present material, we do not observe any $S_2^0$ emission after sample coloration (Figure S24), likely due to the very intense blue-emitting Ti-related species already present in the material. We observed photochromism only for a reduced material, i.e. when the original sulphates have reduced to disulphides, which furthermore suggests that the disulfide may be the PC species.

In summary, the suggested mechanism for tenebrescence (Figure 7e) is as follows: (1) UV excitation of the $S_{2-}$ ion results in an electron transfer to $Sm^{3+}$, yielding $S_2^0$, and $Sm^{2+}$. (2) The latter absorbs in the visible range, creating the gray color. (3) With the help of thermal energy, the electron escapes from $Sm^{2+}$ to the conduction band and returns to the disulfide. (4) This results in the initial $Sm^{3+}/S_2^-$ pair and the return to the original white color.

Finally, since the tenebrescence excitation of sample LiSod:0.01Sm (Figure 7d) overlaps significantly with the UV region of the solar spectrum, it was theorized that different UV indices (UVIs) would yield different photochromic responses from the material; more specifically, a higher UV index would induce stronger coloration [18]. To test this, the reflectance of the material was measured across a range of UVIs under a solar simulator lamp, as illustrated in Figure 7f. The plot shows an approximately linear relationship between UVI and coloration intensity, suggesting potential applications in UV dosimetry. This, combined with the rapid coloration and long bleaching time shown in Figure 6b,c, respectively, indicates that the material has potential for UVI determination in combination with third-party software, such as Sensoglow, an Android application developed at the University of Turku [56]. From this, it can be used as an indicator of whether to use sun protection [18, 57]. Previous studies have shown that other, more traditional hackmanite derivatives are also suited for this application [18, 57].

It should also be noted that the measurements were conducted from lowest to highest UV index. As a result, the increase in coloration across consecutive measurements provides a strong indication of its high fatigue resistance. That said, specific cycling measurements would need to be performed to validate this [57].

## 3 | Conclusion

In this study, we have shown that it is possible to incorporate photochromic sodalites with emissive lanthanide ions, in particular $Sm^{3+}$, $Eu^{3+}$, $Tb^{3+}$, and $Dy^{3+}$. Doping was achieved by adding a $LiAlSiO_4$ precursor before sodalite formation, resulting in a sodalite structure with minimal changes to the host lattice. Although the typical f-f emission of lanthanides was predominantly masked by other luminescent impurities, such as $Ti^{3+}$, the reducing conditions used in the synthesis led to new optical properties emerging, particularly in europium- and samarium-doped systems.

Europium-doped hackmanite resulted in the formation of both $Eu^{2+}$ and $Eu^{3+}$, resulting in green persistent luminescence lasting up to about 40 min, due to $Eu^{2+}$ 5d-4f transitions—to our knowledge, the first observation of this type of luminescence in hackmanites. Thermoluminescence measurements revealed the presence of both shallow and deep electron traps, the former being responsible for the persistent luminescence observed at room temperature. This room-temperature persistent luminescence gives this material potential applications in lighting.

In contrast, doping with samarium resulted in a material with an unusual photochromic response, characterized by a reflectance minimum in the NIR (780 nm) and bleaching dominated by thermal rather than optical processes. It was suggested through spectroscopic data that the samarium dopant plays a key role in the tenebrescence mechanism via reversible $Sm^{3+}/Sm^{2+}$ redox chemistry, coupled to disulphide photochromic centers—a mechanism distinguishable from traditional hackmanites. In addition, the material showed a linear relationship between the UV index and photochromic response, highlighting its potential for UV sensing.

Overall, this work has shown that lanthanide doping can modulate both luminescence and photochromism in hackmanites, highlighting and expanding the versatility of this class of material.

## 4 | Experimental Methods

### 4.1 | Synthesis

The lithium aluminosilicates ($Li_{1-x}AlSiO_4$:$xLn^{3+}$, $x$ = 0–0.06) were synthesized via a solid-state method adapted from Gokhe et al. [28]. The anhydrous reagents, $Li_2CO_3$ (Thermo Scientific, >99%), $Al_2O_3$ (Sigma–Aldrich, 99.99%), fumed $SiO_2$ (Sigma–Aldrich, product number S5505) and $Ln_2O_3$ (Ln = Sm (Typpi Oy Oulu, 99%), Eu (International Laboratory USA, 99.99%), Tb (International Laboratory USA, 99.99%), or Dy (International Laboratory USA, 99.9%)) were weighed stoichiometrically and transferred to a Philips PW4018/00 MiniMill Planetary Ball Mill with a small quantity of acetone, adopting $H_3BO_3$ (J.T.Baker, ≥99.5%) as a flux (approximately 10% of the total reagent mass). The materials were then thoroughly mixed by ball milling for 2 h at 3–6 g. The resulting slurry was dried in an oven at approximately 70°C to ensure all acetone had evaporated, then transferred to an alumina boat. The powder was then heated in air at 800°C for 4 h, with a heating rate of approximately 10°C $min^{-1}$. Upon cooling to room temperature, the resulting powder was re-ground and heated in air at 900°C for 4 h with a heating rate of approximately 10°C $min^{-1}$ to yield a white powder.

All sodalite derivatives (LiSod:$x$Ln) were synthesized via a solid-state method adapted from experiments conducted by Byron et al. [7]. The $Ln^{3+}$-doped aluminosilicate, anhydrous NaCl (Fischer Scientific, ≥99.5%), and anhydrous $Na_2SO_4$ (Sigma–Aldrich, >99.0%) were ground together in an agate mortar and then initially heated in air at 850°C for 5–7 h with a heating rate of approximately 3°C $min^{-1}$. Once cooled, the powder was re-ground and placed in the same alumina boat for heating in air or under a reducing atmosphere (10% $H_2$, 90% $N_2$). Once purged, the sample was heated at 850°C for 2 h with a heating rate of approximately 18°C $min^{-1}$. The resulting powder was ground and washed several times with distilled water to remove soluble impurities. The remaining powder was separated from the water using a Heraeus

Instruments Biofuge Stratos centrifuge at 2500 rpm. Samples in the $Eu^{2+}$ series (LiSod:0.02Eu—LiSod:0.06Eu) were not washed.

## 4.2 | Characterization

The XRD patterns obtained throughout this project were recorded on a PANalytical Aeris powder X-ray diffractometer. The samples were prepared on a zero-background silicon disc, utilizing X-rays with a wavelength of 1.5406 Å (Cu K$\alpha$). Rietveld refinements were carried out using PANalytical HighScore software (version 4.9.0.27512) utilizing the PDF-4 + 2023 4.21.0.2 database.

XRF spectra were recorded using a PANalytical Epsilon 1 XRF spectrometer employing a silver anode X-ray tube. Samples were measured as loose powders using a 1 h program comprising four separate measurements. The results are quantified by automatic deconvolution using the internal Omnian calibration.

The SEM-EDS maps were obtained using the Thermo Fisher Scientific Apreo S field-emission scanning electron microscope equipped with Oxford Instruments UltimMax 100 energy dispersive spectrometer under low vacuum conditions (90 Pa $H_2O$) at 15 kV accelerating voltage. Samples were prepared for elemental mapping by suspending a small quantity of each sample in an epoxy resin cast (Petropoxy 154, Burnham Petrographics). The targeted area for imaging was first polished manually using silicon carbide sandpapers of varying grades and then using a Hitachi ArBlade 5000 broad argon ion beam mill to achieve a flat, smooth surface with adequate particle exposure.

Luminescence spectra were recorded using an Edinburgh Instruments FLS1000 Photoluminescence Spectrometer. A long-pass emission filter was installed to prevent undesired reflections from reaching the detector, with the cut-on wavelength selected according to the excitation wavelength used. Luminescence excitation spectra were also recorded using this instrument, although no filters were used during these measurements. Certain luminescence spectra, primarily those of LiSod:0.01Ln samples upon high-energy UV excitation (250–290 nm), were instead recorded using a Cary Varian Eclipse Fluorescence Spectrophotometer in phosphorescence mode, with a Hamamatsu R928 photomultiplier tube detector and a 150 W xenon lamp as the source. Samples were packed into the metal sample holder, over which a small piece of quartz glass was secured. Additionally, photographs of the emission from each sample were taken with a Canon EOS 250D DSLR camera.

Persistent luminescence spectra were recorded using the same Cary Varian Eclipse Fluorescence Spectrophotometer. Samples were prepared as above, then excited for 5 min at 365 nm using a UVLS-24 EL Series UV Lamp with an intensity of 2.57 mW $cm^{-2}$. The intensity of the UV radiation was measured using an Opsytec Dr Gröbel RM12 UV-A Sensor connected to an Opsytec Dr Gröbel RM12 Radiometer. The afterglow emission was then measured after a 30-s delay, both to allow the sample to be transferred into the spectrometer and to avoid detector saturation. The instrument was set to Bio/Chemiluminescence mode, with the xenon lamp off and the maximum measurement speed. A large emission bandwidth of 20 nm was used to maximize sensitivity.

Emission decay curves were recorded using an International Light Technologies ILT5000 Research Radiometer connected to a photomultiplier tube. Before measurement, the samples were excited for 5 min at 254 nm using the UVLS-24 EL Series UV Lamp. The photopic luminance was measured until the standard photopic limit of 0.32 mcd $m^{-2}$ was reached.

Thermoluminescence (TL) analysis was carried out using the MikroLab Thermoluminescent Materials Laboratory Reader RA'04. Prior to the measurement, 10 mg of the sample was placed in an Aluminum cup and irradiated at RT for 5 min using a 254 nm hand lamp (UVLS-24 EL, 4 W, 254/365 nm). Measurement began 60 s after ceasing irradiation. If samples were preheated, the measurement began immediately after the samples cooled to RT. For the glow curve analysis, the initial rise method was used [48].

Reflectance spectra under UV excitation were recorded using an Agilent Cary 60 UV-vis Spectrophotometer, equipped with the corresponding Opsytec Dr Gröbel integrating sphere to which the sample holder was attached. Measurements were taken with the device set to reflectance mode, the excitation beam in dual-beam mode, and an averaging time of 0.1 s.

Tenebrescence rise curve measurements were recorded using the AvaSpec-ULS2048LTEC SensLine Thermo-Electric Cooled Fiber-Optic Spectrometer (HS-TEC) connected to an Avantes 600 µm FC-UV600-1-SR fiber optic cable, averaging 5 scans with an integration time of 150 ms. Samples were prepared by depositing a small amount of sample on a PTFE disk, which was smoothed with a glass microscope slide and excited at 254 nm with a UVLS-24 EL Series UV Lamp. The sample was continuously excited throughout the measurement. The area of the resulting reflectance valley between 600 and 1000 nm was measured every 1 s.

Tenebrescence bleaching curve measurements were recorded using the AvaSpec-ULS2048LTEC SensLine Thermo-Electric Cooled Fiber-optic Spectrometer (HS-TEC) connected to a 1000 µm VIS/NIR.037NA PC04 fiber optic cable. Samples were prepared by depositing a small amount of sample on a PTFE disk, which was smoothed with a glass microscope slide and excited with a 254 nm UVLS-24 EL Series UV Lamp for 5 min. The area of the resulting reflectance valley was measured every second between 600 and 1000 nm. The reflectance was measured continuously under illumination from an Ocean Optics HL-2000 Halogen Light Source (116 lux) and from ambient cool white LED ceiling lights (804 lux). Light intensity was measured using a Hagner E4-X Digital Luxmeter.

Absolute tenebrescence excitation spectra were recorded using the AvaSpec-ULS2048LTEC SensLine Thermo-Electric Cooled Fiber-optic Spectrometer (HS-TEC) connected to an Avantes AvaSpec-ULS2048LTEC SensLine Thermo-Electric Cooled Fiber-optic Spectrometer (HS-TEC), averaging 10 scans with an integration time of 160 ms. Samples were prepared by depositing a small amount of sample on a PTFE disk, which was smoothed with a glass microscope slide and excited with 200–400 nm UV radiation in 20 nm increments produced by an SB522 150 W Xe-arc lamp coupled to a LOT MSH 300 monochromator. Samples were

excited for 7.5 min at each wavelength, and a fresh, uncolored sample was used for each measurement to ensure no residual coloration from the previous measurement. The individual values in the spectra were obtained by integrating the reflectance valley between 600 and 1000 nm.

Thermotenebrescence measurements were conducted using a combination of a Mikrolab Laboratory Reader-Analyser RA'04 thermoluminescence reader/analyzer and an Avantes AvaSpec-ULS2048LTEC SensLine Thermo-Electric Cooled Fiber-optic Spectrometer (HS-TEC). The thermoluminescence instrument was used as a heating element, heating the sample from room temperature to 400°C at 3°C $s^{-1}$, and the spectrometer, connected to a FCR-7UVIR400-2-BX-6×350-HTX heat-resistant fiber-optic cable, was used to measure the reflectance of the sample upon both heating and UV excitation. Samples were excited with a 254 nm UVLS-24 EL Series UV Lamp. The reflectance signal was corrected for heating effects on an uncolored sample and for spontaneous fading. The reflectance curves were integrated over 600–1000 nm to determine the color intensity at each temperature. The resulting integrals were plotted against temperature, and the activation energy of thermal bleaching was calculated using the initial rise method [48].

XPS survey and core-level spectra were collected using the Thermo Scientific Nexsa XPS system equipped with a monochromatic Al K$\alpha$ X-ray source and HeI/II UV discharge lamp. The presented core-level spectra were scanned using a 400 mm X-ray spot size and 50 eV pass energy. The binding energy scale was calibrated with the C 1s C—C component set to 284.8 eV.

Reflectance spectra upon solar radiation excitation were recorded using the CM-2600d Spectrophotometer from Konica Minolta Sensing. Samples were prepared by depositing a small amount of sample on a PTFE disk, which was smoothed with a glass microscope slide and exposed to solar radiation of varying UV indices for 5 min, as confirmed using a Solarmeter Digital Ultraviolet Radiometer Model 6.5. The solar radiation was provided by a LOT Quantum Design solar simulator (LS0500/1). Reflectance spectra were recorded before and after irradiation, and the difference between the two curves was calculated at 740 nm, the upper detection limit of the measurement device, closest to the reflectance minimum. The sample was left in daylight by an outside window between measurements to allow it to return to its colorless state prior to measurement. The resulting differences were plotted against the UV index.


### Acknowledgements

Research Council of Finland (project #361161) as well as Jane and Aatos Erkko Foundation and the Technology Industries of Finland Centennial Foundation (co-funders of the JÄMOMAT project) are acknowledged for funding. Universities of Durham and Turku are thanked for the undergraduate student exchange programme (F102). The Materials Research Infrastructure (MARI) at University of Turku, is acknowledged for access and support with the SEM and XPS facilities.

Open access publishing facilitated by Turun yliopisto, as part of the Wiley - FinELib agreement.

### Funding

Research Council of Finland (project #361161), Jane and Aatos Erkko Foundation, together with the Technology Industries of Finland Centennial Foundation (JÄMOMAT project).


### Conflicts of Interest

The authors declare no conflicts of interest.

### Data Availability Statement

The data that support the findings of this study are available from the corresponding author upon reasonable request.

### References


1. J. Abe, H. Yamashita, and K. P. I. Mutoh, "Photochromism," in *Encyclopedia of Polymeric Nanomaterials*, ed. S. Kobayashi and K. Müllen, (Springer, 2015), https://doi.org/10.1007/978-3-642-29648-2_119.⟨/bib.

2. V. A. Barachevsky, "Photochromic Organic and Hybrid Nanomaterials," in *2D Nanomaterials for Energy Applications*, ed. S. Zafeiratos, (Elsevier, 2020), https://doi.org/10.1016/B978-0-12-816723-6.00007-1.⟨/bib.

3. A. B. A. Kayani, S. Kuriakose, M. Monshipouri, et al., "UV Photochromism in Transition Metal Oxides and Hybrid Materials," *Small* 17, no. 32 (2021): 2100621, https://doi.org/10.1002/smll.202100621.

4. R. Pardo, M. Zayat, and D. Levy, "Photochromic Organic–Inorganic Hybrid Materials," *Chemical Society Reviews* 40, no. 2 (2011): 672–687, https://doi.org/10.1039/C0CS00065E.

5. P. Colinet, H. Byron, S. Vuori, et al., "The Structural Origin of the Efficient Photochromism in Natural Minerals," *Proceedings of the National Academy of Sciences* 119, no. 23 (2022): 2202487119, https://doi.org/10.1073/pnas.2202487119.

6. S. Vuori, P. Colinet, I. Norrbo, et al., "Detection of X-Ray Doses With Color-Changing Hackmanites: Mechanism and Application," *Advanced Optical Materials* 9, no. 20 (2021): 2100762, https://doi.org/10.1002/adom.202100762.

7. H. C. Byron, C. Swain, P. Paturi, et al., "Highly Tuneable Photochromic Sodalites for Dosimetry, Security Marking and Imaging," *Advanced Functional Materials* 2303398, https://doi.org/10.1002/adfm.202303398.

8. F. Blumentritt, C. Latouche, Y. Morizet, M.-T. Caldes, S. Jobic, and E. Fritsch, "Unravelling the Origin of the Yellow-Orange Luminescence in Natural and Synthetic Scapolites," *The Journal of Physical Chemistry Letters* 11, no. 12 (2020): 4591–4596, https://doi.org/10.1021/acs.jpclett.0c00712.

9. A. Armstrong and T. Weller, "New Sodalite Frameworks; Synthetic Tugtupite and a Beryllosilicate Framework With a 3: 1 Si ? Be Ratio," *Dalton Transactions* 0, no. 24 (2006): 2998–3005, https://doi.org/10.1039/B600579A.

10. P. Colinet and A. Gheeraert, "On the Spectroscopic Modeling of Localized Defects in Sodalites by TD-DFT," *The Journal of Physical Chemistry C* 124, no. 16 (2020): 8949–8957, https://doi.org/10.1021/acs.jpcc.0c00615.

11. R. Shannon, "Revised Effective Ionic Radii and Systematic Studies of Interatomic Distances in Halides and Chalcogenides," *Acta Crystallographica Section A* 32 (1976): 751–767, https://doi.org/10.1107/S0567739476001551.

12. W. Phillips, "Properties of Cathodochromic Sodalite," *Journal of The Electrochemical Society* 117, no. 12 (1970): 1557, https://doi.org/10.1149/1.2407383.

13. H. Byron, I. Norrbo, and M. Lastusaari, "A Zeolite-Free Synthesis of Luminescent and Photochromic Hackmanites," *Journal of Alloys and Compounds* 872 (2021): 159671, https://doi.org/10.1016/j.jallcom.2021.159671.

14. M. Gaft, G. Panczer, L. Nagli, and H. Yeates, "Laser-Induced Time-Resolved Luminescence of Tugtupite, Sodalite and Hackmanite," *Physics and Chemistry of Minerals* 36, no. 3 (2009): 127–141, https://doi.org/10.1007/s00269-008-0263-1.

15. A. Sidike, A. Sawuti, X.-M. Wang, et al., "Fine Structure in Photoluminescence Spectrum of $S_2^-$ Center in Sodalite," *Physics and Chemistry of Minerals* 34, no. 7 (2007): 477–484, https://doi.org/10.1007/s00269-007-0161-y.

16. I. Norrbo, J. M. Carvalho, P. Laukkanen, et al., "Lanthanide and Heavy Metal Free Long White Persistent Luminescence From Ti Doped Li–Hackmanite: A Versatile, Low-Cost Material," *Advanced Functional Materials* 27, no. 17 (2017): 1606547, https://doi.org/10.1002/adfm.201606547.

17. I. Norrbo, P. Gluchowski, I. Hyppänen, et al., "Mechanisms of Tenebrescence and Persistent Luminescence in Synthetic Hackmanite $Na_8Al_6Si_6O_{24}(Cl,S)_2$," *ACS Applied Materials & Interfaces* 8, no. 18 (2016): 11592–11602, https://doi.org/10.1021/acsami.6b01959.

18. I. Norrbo, A. Curutchet, A. Kuusisto, et al., "rom the Assessment of the Fundamental Properties to the Device," *Materials Horizons* 5, no. 3 (2018): 569–576, https://doi.org/10.1039/C8MH00308D.

19. S. Shionoya, W. M. Yen, eds. 1999, *Phosphor Handbook*, CRC Press.

20. J. E. Geusic, H. M. Marcos, and L. G. Van Uitert, "Laser Oscillations in Nd-DOPED Yttrium Aluminum, Yttrium Gallium and Gadolinium Garnets," *Applied Physics Letters* 4 (1964): 182–184, https://doi.org/10.1063/1.1753928.

21. R. J. Mears, L. Reekie, I. M. Jauncey, and D. N. Payne, "Low-Noise Erbium-Doped Fibre Amplifier Operating at 1.54 μm," *Electronics Letters* 23, no. 19 (1987): 1026–1028, https://doi.org/10.1049/el:19870719.

22. I. Norrbo, I. Hyppänen, and M. Lastusaari, "Up-Conversion Luminescence—A New Property in Tenebrescent and Persistent Luminescent Hackmanites," *Journal of Luminescence* 191 (2017): 28–34, https://doi.org/10.1016/j.jlumin.2017.02.046.

23. M. Yu, D. Luo, J. Kuang, and W. Yuan, "Synthesis and Luminescence Properties of $Eu^{3+}$ Doped Sodalite Phosphors Using Kaolin," *Results in Physics* 41 (2022): 105887, https://doi.org/10.1016/j.rinp.2022.105887.

24. M. Kaiheriman, A. Sidike, A. Maimaitinasier, A. Reheman, and B. Rouzi, "Photoluminescence Properties of $Tb^{3+}$-Doped Sodalite Under VUV–UV Light Excitation," *Journal of Luminescence* 157 (2015): 411–415, https://doi.org/10.1016/j.jlumin.2014.08.028.

25. Z. Yang, J. Du, L. I. D. J. Martin, D. Van der Heggen, and D. Poelman, "Highly Responsive Photochromic Ceramics for High-Contrast Rewritable Information Displays," *Laser & Photonics Reviews* 15, no. 4 (2021): 2000525, https://doi.org/10.1002/lpor.202000525.

26. J. Zhang, H. Lin, and J. Du, "Realizing Color-Tunable Photochromism in Apatite-Structured Compounds via Trapping Energy Management for Wide Gamut Encryption," *Laser & Photonics Reviews* 19, no. 16 (2025): 2500221, https://doi.org/10.1002/lpor.202500221.

27. J. Shao, S. Feng, M. Liu, et al., "Promising Coloration Composite Strategy to Multicolor Photochromism for On-Demand Information Displays," *Advanced Functional Materials* 35, no. 27 (2025): 2425059, https://doi.org/10.1002/adfm.202425059.

28. U. B. Gokhe, K. A. Koparkar, and S. K. Omanwar, "Synthesis and Photoluminescence Properties of Near-UV Pumped Novel $Sm^{3+}$ Doped B-$LiAlSiO_4$ Phosphor for Red-Orange Leds," *Journal of Alloys and Compounds* 689 (2016): 992–997, https://doi.org/10.1016/j.jallcom.2016.08.057.

29. W. Zhao, X. Feng, C. Zhang, and Y. Zhang, "Improvement in the Luminescence and Enhancement of the Thermo-Stability of $SiO_2$ Coating on $LiAlSiO_4$:$Eu^{3+}$ Phosphor," *Applied Physics A* 128 (2022): 401, https://doi.org/10.1007/s00339-022-05537-6.

30. D. Umamaheswari, B. C. Jamalaiah, T. Sasikala, I.-G. Kim, and L. R. Moorthy, "Photoluminescence Properties of $Sm^{3+}$-Doped SFB Glasses for Efficient Visible Lasers," *Journal of Non-Crystalline Solids* 358, no. 4 (2012): 782–787, https://doi.org/10.1016/j.jnoncrysol.2011.12.023.

31. C.-L. Yu, G.-H. Liu, D.-B. Jin, et al., "Peculiar $\beta$-$Li_2TiO_3$: $Eu^{3+}$ Red Light Emitting Dominated by Electric Dipole Transition: Asymmetric Lattice Point Regulation and Luminescence Performance," *Journal of Alloys and Compounds* 973 (2024): 172917, https://doi.org/10.1016/j.jallcom.2023.172917.

32. S. Nan, F. Hong, H. Xu, et al., "Luminescence Properties and Energy Transfer of $Tb^{3+}$, $Eu^{3+}$ Co-Doped $YTaO_4$ Phosphors Obtained via Sol–Gel Combustion Process," *Journal of Materials Science: Materials in Electronics* 31, no. 16 (2020): 13688–13695, https://doi.org/10.1007/s10854-020-03926-2.

33. U. Caldiño, E. Álvarez, A. Speghini, and M. Bettinelli, "Cold and Warm White Light Generation Using $Zn(PO_3)_2$ Glasses Activated by $Ce^{3+}$," *Journal of Luminescence* 132, no. 8 (2012): 2077–2081, https://doi.org/10.1016/j.jlumin.2012.03.045.

34. A. Alemi, S. Khademinia, S. W. Joo, et al., "Hydrothermal Synthesis and Investigation of Optical Properties of $Nb^{5+}$-Doped Lithium Silicate Nanostructures," *International Nano Letters* 4, no. 1 (2014): 4, https://doi.org/10.1186/2228-5326-4-4.

35. National Institute of Standards and Technology, "Neutron Cross Sections," accessed April 02 (2026), https://www.ncnr.nist.gov/resources/activation/scattering_table.html#sm.

36. T. F. W. Barth, "The Structures of the Minerals of the Sodalite Family," *Zeitschrift Für Kristallographie* 83 (1932): 405–414, https://doi.org/10.1524/zkri.1932.83.1.405.

37. M. R. MacDonald, J. E. Bates, J. W. Ziller, F. Furche, and W. J. Evans, "Completing the Series of +2 Ions for the Lanthanide Elements: Synthesis of Molecular Complexes of $Pr^{2+}$, $Gd^{2+}$, $Tb^{2+}$, and $Lu^{2+}$," *Journal of the American Chemical Society* 135, no. 26 (2013): 9857–9868, https://doi.org/10.1021/ja403753j.

38. C. Agamah, S. Vuori, P. Colinet, et al., "Hackmanite—The Natural Glow-in-the-Dark Material," *Chemistry of Materials* 32, no. 20 (2020): 8895–8905, https://doi.org/10.1021/acs.chemmater.0c02554.

39. M. Vigier, E. Fritsch, T. Cavignac, C. Latouche, and S. Jobic, "Shortwave UV Blue Luminescence of some Minerals and Gems due to Titanate Groups," *Minerals* 13, no. 1 (2023): 104, https://doi.org/10.3390/min13010104.

40. P. Dorenbos, "The $Eu^{3+}$ Charge Transfer Energy and the Relation With the Band Gap of Compounds," *Journal of Luminescence* 111, no. 1 (2005): 89–104, https://doi.org/10.1016/j.jlumin.2004.07.003.

41. F. Clabau, X. Rocquefelte, S. Jobic, et al., "On the Phosphorescence Mechanism in $SrAl_2O_4$: $Eu^{2+}$ and Its Codoped Derivatives," *Solid State Sciences* 9, no. 7 (2007): 608–612, https://doi.org/10.1016/j.solidstatesciences.2007.03.020.

42. E. R. Williams, A. Simmonds, J. A. Armstrong, and M. T. Weller, "Compositional and Structural Control of Tenebrescence," *Journal of Materials Chemistry* 20, no. 48 (2010): 10883–10887, https://doi.org/10.1039/C0JM02066D.

43. T. Le Bahers, M. Lastusaari, M. Weller, and H. Friis, "Photochromic Sodalites: From Natural Minerals to Advanced Applied Materials," *Accounts of Chemical Research* 58, no. 3 (2025): 330–341, https://doi.org/10.1021/acs.accounts.4c00624.

44. I. Hassan, S. M. Antao, and J. B. Parise, "Sodalite: High-Temperature Structures Obtained From Synchrotron Radiation and Rietveld Refinements," *American Mineralogist* 89 (2004): 359–364, https://doi.org/10.2138/am-2004-2-315.

45. D. Taylor, "Cell Parameter Correlations in the Aluminosilicate-Sodalites," *Contributions to Mineralogy and Petrology* 51, no. 1 (1975): 39–47, https://doi.org/10.1007/BF00403511.

46. M. T. Weller and G. Wong, "Characterisation of Novel Sodalites by Neutron Diffraction and Solid-State NMR," *Solid State Ionics* 32–33 (1989): 430–435, https://doi.org/10.1016/0167-2738(89)90251-8.

47. H. Byron, T. Kreivilä, P. Colinet, T. L. Bahers, and M. Lastusaari, "New Shades of Photochromism—Yellow Sodalites for the Detection of Blue Light," *Journal of Materials Chemistry C* 11, no. 9 (2023): 3360–3374, https://doi.org/10.1039/D3TC00116D.

48. S. W. S. McKeever, "Basic Methods for Evaluating Trapping Parameters," in *Thermally and Optically Stimulated Luminescence* (John Wiley & Sons, 2011), https://doi.org/10.1002/9781119993766.ch5.

49. D. Liu, F. Niu, X. Zhang, L. Shen, and Y. Yang, "Calciothermic Reduction Reaction Behavior and Samarium Ion Valence Evolution of $SmF_3$," *Mining, Metallurgy & Exploration* 41 (2024): 1619–1627, https://doi.org/10.1007/s42461-024-01044-9.

50. A. Meléndez-Sans, V. M. Pereira, C. F. Chang, et al., "Influence of Nitrogen Stoichiometry and the Role of Sm 5d States in SmN Thin Films," *Physical Review B* 110, no. 4 (2024): 045120, https://doi.org/10.1103/PhysRevB.110.045120.

51. D. Labou and S. G. Neophytides, "Combined XPS, Electrochemical and Kelvin Probe Measurements of NaY Zeolite," *Solid State Ionics* 177, no. 11 (2006): 971–977, https://doi.org/10.1016/j.ssi.2006.03.014.

52. J. Du, Z. Yang, H. Lin, and D. Poelman, "Inorganic Photochromic Materials: Recent Advances, Mechanism, and Emerging Applications," *Responsive Materials* 2, no. 2 (2024): 20240004, https://doi.org/10.1002/rpm.20240004.

53. A. Curutchet and T. Le Bahers, "Modeling the Photochromism of S-Doped Sodalites Using DFT, TD-DFT, and SAC-CI Methods," *Inorganic Chemistry* 56, no. 1 (2017): 414–423, https://doi.org/10.1021/acs.inorgchem.6b02323.

54. P. Dorenbos, "Systematic Behaviour in Trivalent Lanthanide Charge Transfer Energies," *Journal of Physics-Condensed Matter* 15, no. 49 (2003): 8417, https://doi.org/10.1088/0953-8984/15/49/018.

55. Y. S. Zavorotny, E. V. Lutsko, A. O. Rybaltovskii, P. V. Chernov, V. O. Sokolov, and R. R. Khrapko, "Color Centers in Sulfur-Doped Silica Glass: Spectroscopic Manifestations of an Interstitial Molecule S2," *Glass Physics and Chemistry* 27, no. 4 (2001): 331–336, https://doi.org/10.1023/A:1011364126241.

56. S. Vuori, T. Laine, I. Norrbo, J. Holvitie, and M. Lastusaari, "Sensoglow - An Android Application for Determining UV Index and UV Dose from Hackmanite," *University of Turku, Finland* (2024).

57. A. Lawrynowicz, S. Vuori, E. Palo, M. Winther, M. Lastusaari, and K. Miettunen, "Transforming Fabrics Into UV-Sensing Wearables: A Photochromic Hackmanite Coating for Repeatable Detection," *Chemical Engineering Journal* 494 (2024): 153069, https://doi.org/10.1016/j.cej.2024.153069.

## Supporting Information

Additional supporting information can be found online in the Supporting Information section.

**Supporting File:** adom71326-sup-0001-SuppMat.docx.